

Asymmetric Assembly of Lennard-Jones Janus Dimers

Sina Safaei,^{1,2} Caleb Todd,² Jack Yarnley,² Shaun Hendy,^{1,2,3} and Geoff R. Willmott^{1,2,4}

¹*The MacDiarmid Institute for Advanced Materials and Nanotechnology, New Zealand*

²*Department of Physics, University of Auckland, New Zealand*

³*Te Pūnaha Matatini, Department of Physics, University of Auckland, New Zealand*

⁴*School of Chemical Sciences, University of Auckland, New Zealand*

Self-assembly of Janus (or ‘patchy’) particles is dependent on the precise interaction between neighbouring particles. Here, the orientations of two amphiphilic Janus spheres within a dimer in an explicit fluid are studied with high geometric resolution. Molecular dynamics simulations and first-principles energy calculations are used with hard- and soft-sphere Lennard-Jones potentials, and temperature and hydrophobicity are varied. The most probable centre-centre-pole angles are in the range 40° to 55° , with pole-to-pole alignment not observed due to orientational entropy. Angles near 90° are energetically unfavoured due to solvent exclusion, and the relative azimuthal angle between the spheres is affected by solvent ordering.

Janus particles (JPs) are micro- or nanoparticles that have at least two sides with distinct physical or chemical properties [1–5]. JPs can have asymmetry in (for example) optical, electrical, or magnetic properties; they can be synthesised with different shapes (e.g. spheroids, rods, platelets); and properties can be altered over particular areas, resulting in ‘patchy’ particles. Amphiphilic microspheres, which have different wettability on each hemisphere, are a commonly-studied type of JP [6–11].

Directional interactions between JPs can lead to self-assembly of complex structures [3, 4, 12], and there has been extensive interest in related design rules for Janus and patchy particles [13–16]. In 3D, experiments have produced aggregates ranging from small clusters up to non-equilibrium helices with variable chirality [8]. Simulations have predicted phases including small clusters [17], micellar or wire-like structures [17–21], and sheets [11, 18]. In 2D, close-packed particles [22, 23] can produce tiled patterns [24–26], while less dense arrangements include clusters [26], chains [27] and open lattices [28]. Phases depend on parameters such as solvent properties, temperature, and patch geometry [21, 29].

An analogy can be made between particle self-assembly and formation of chemical bonds, albeit with different geometric rules [14, 30, 31] that are yet to be fully understood. For example, the number and directions of ‘bonds’ can be controlled via the positions and sizes [13, 14, 16, 26, 28, 30] of patches. Orientational entropy determines the flexibility (or ‘floppiness’) of bonds [8, 14, 24, 28, 30], and can determine the stability of a phase [28, 30–34].

The precise nature of interactions between particles ultimately determines the possible aggregates. Simulations are an important predictive tool in this field [14], and a variety of anisotropic directionally-dependent point potentials have been used to study JP assembly [22]. These potentials typically consist of an isotropic repulsion such as an infinitely large ‘hard-sphere’ potential barrier [11, 18, 35, 36], as well as an anisotropic interaction representing the JP asymmetry. Kern and

Frenkel’s approach [36], which has been widely used [11, 18, 22, 24, 25, 27, 28], applies a square-well potential when attractive surfaces are in contact on the line joining the centres of two particles, and zero otherwise. This is suitable for modelling short-range forces, and produces an energetic step function with respect to JP orientation at the boundary of a hemisphere (or patch). As an alternative, the energy can be minimised when attractive hemispheres are in pole-to-pole contact, and increase according to vector dot products as the JPs are rotated [17, 19, 22, 35]. These potentials have been simplified for the purpose of many-body calculations. There are limited examples of more detailed geometric calculations of the energy between two JPs, in which the interaction has been based on electrostatics (i.e. DLVO theory) [37, 38] and critical Casimir forces [39, 40].

In this Letter, we study the 3D orientation dynamics of amphiphilic spherical JPs in self-assembled dimers. We use a Lennard-Jones potential and two geometrically rigorous calculation methods; none of these features have appeared in previous studies of the interaction between two JPs. Results obtained using molecular dynamics (MD) simulations of many-atom JPs are presented alongside calculations made using a numerical integration (NI) method we have developed. In the latter method, JP hemispheres are modelled as continuous surfaces, and potentials are integrated to calculate the first-principles interaction energy for any particular configuration. An analytic equivalent of our NI method has been used to model other Lennard-Jones nanostructures [41] including uniform spheres [42], but to our knowledge this has not been applied to Lennard-Jones JPs.

Put together, our results produce a detailed and nuanced description of particle interactions for short-ranged potentials, and specifically the Lennard-Jones potential which approximates van der Waals forces. The MD and NI approaches both directly include solvent, have non-zero separation of JP and solvent surfaces, and can account for orientational entropy. In addition, the MD supports study of solvent ordering, changing surface sepa-

ration lengths, and other dynamics. Results from MD and NI are broadly consistent at different temperatures and hydrophobicities, enabling discussion of the geometric and entropic contributions to the preferred orientations of JPs in a dimer. Aside from improving fundamental understanding in this way, the results can inform the development of design rules in self-assembled structures using ‘floppy’ bonds. Dimers of JPs are particularly important because they are the first kinetic step in any self-assembly [8], they are possible stand-alone modular building blocks, and they appear as a motif in 2D tiling [24–26].

Molecular dynamics - MD simulations were carried out using the large-scale atomic molecular massively parallel simulator (LAMMPS), and the open visualisation tool (OVITO) was employed for visualisation and analysis of the results [43, 44]. All simulations were performed in Lennard-Jones reduced units, where σ is the unit of distance, ϵ the unit of energy, m the unit of mass and τ the unit of time ($\sqrt{m\sigma/\epsilon}$), without loss of generality. The equations of motion were integrated using the standard velocity-Verlet algorithm with a timestep of $\Delta t = 0.01 \tau$. All simulations were carried out in a canonical ensemble (NVT) in which the temperature was set at $1.1 \epsilon/k_B$ and controlled by a Langevin thermostat with a damping parameter of 10τ (for methodological details, see the Supplemental Material [45]).

MD studies of JPs can typically be categorised into those which model Janus particles as single ‘atoms’ using point potentials [17, 20, 22, 46] or those which represent spherical JPs as collections of atoms distributed over the sphere’s surface (Fig. 1(a)) [47–51]. A many-atom JP can be used to rigorously study hydrodynamics such as the effect of slip on particle rotation and translation [51–54]. Therefore, Janus spheres were modelled as in our previous studies [50, 51], where the atoms were distributed over the surface of the spheres with a surface density of $1.3 \sigma^{-2}$. The positions of atoms were randomised for each simulation, avoiding artefacts associated with regular structures (see the Supplemental Material [45]). Anisotropy of JPs emerges by defining different potentials for atoms on different parts of the surface. Hence, the spheres were divided geometrically into two hemispheres referred to as **1** and **2**, and they interacted with atoms of an explicit solvent referred to as **0**. To design the spheres as similarly as possible to experimentally fabricated JPs, the boundary between the hemispheres is not sharp. This eliminates any related effects [51] and means that the number of atoms on different hemispheres may not be equal.

The potential between atoms separated by distance r was a 12-6 Lennard-Jones potential,

$$U_{ij}(r) = 4\epsilon \left[\left(\frac{\sigma}{r} \right)^{12} - \left(\frac{\sigma}{r} \right)^6 \right], \quad (1)$$

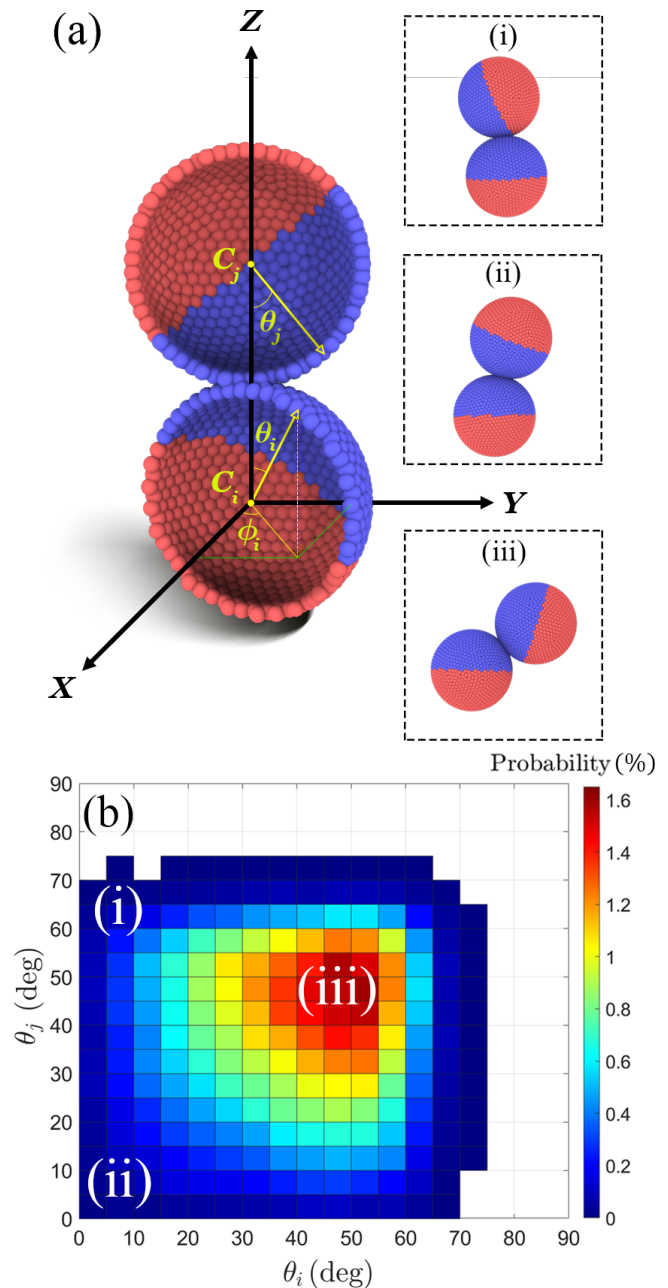


FIG. 1. (a) A dimer of Janus spheres showing the polar angles θ_i and θ_j and the azimuthal angle ϕ_i . The angle $\phi_j = 90^\circ$ is omitted for clarity. C_i and C_j are the centres of the spheres, and the vectors connect the centres to hydrophobic poles. Insets illustrate sphere orientations at specified points on plot (b). (b) The occurrence probability of θ_i and θ_j at $T = 1.1 \epsilon/k_B$, $A = 0.05 \epsilon$, and $R = 10 \sigma$.

with the interaction strengths between different types of atoms defined as:

$$\begin{cases} \epsilon_{(1-0)} = A_o \epsilon_{(0-0)} \\ \epsilon_{(2-0)} = A_i \epsilon_{(0-0)} \\ 0.05 \leq A_o \leq A_i \leq 1.00. \end{cases}$$

Here A (the ‘interaction strength’) is a parameter allowing the potential to be adjusted for the hydrophobic (A_o) and hydrophilic (A_i) hemispheres in a Janus sphere, which are depicted in all figures as blue and red, respectively. As the interaction strength increases, the hydrophobicity of the surface decreases. The interactions $\epsilon_{(1-1)}$, $\epsilon_{(2-2)}$, and $\epsilon_{(1-2)}$ were calculated using the Berthelot mixing rule. Parameters m and σ were the same for all atom types.

To study the orientation of individual JPs in a dimer, two spherical coordinate systems ($r_{i,j}$, $\theta_{i,j}$, $\phi_{i,j}$) were employed (Fig. 1(a)), where the origins are at the centres of each of the spheres $C_{i,j}$, and the line connecting the centres ($\overrightarrow{C_i C_j}$) indicates the direction of the z -axis. The orientation of each sphere is defined by a vector connecting its centre to its hydrophobic pole. The axes are defined so that $\phi_j = 90^\circ$ and the relative orientation of the two Janus spheres can be fully specified using θ_i , θ_j , and $\Delta\phi$ (where $\Delta\phi = \phi_j - \phi_i$).

Fig. 1(b) is an example of a simulated occurrence probability distribution as a function of the polar angles θ_i and θ_j . Here, the observed angles are most commonly in the range from 30° to 60° , and orientations with angles higher than 75° are not observed. Orientations with angles less than 30° are not favoured due to the lower available surface area at those angles - this is the effect of orientational entropy. The sudden decrease above 60° is related to screening of solvent atoms from the hydrophobic hemispheres, as discussed below.

Numerical integration - In the numerical integration (NI) approach, we calculated the interaction between two Janus spheres over a range of configurations. Each sphere consisted of two continuous hemispherical surfaces separated by a uniform, equatorial boundary. The energy at any given configuration was calculated by integrating the Lennard-Jones interaction over the different geometries, resulting in a total of 8 integrals (4 surface-surface and 4 surface-solvent). In addition to the hard-sphere (12-6) potential in Eq. 1, we carried out calculations using a soft-sphere (9-6) Lennard-Jones potential. This was of interest due to frequent use of soft directional-dependent potentials in previous studies of Janus spheres [19, 55–61].

The centres of the two spheres were positioned at $(0, 0, 0)$ and $(0, 0, 2R + d_s)$ in Cartesian coordinates (Fig. 1(a)), where R is the sphere radius and d_s is the distance between the spheres’ surfaces. A fixed distance between the solid surfaces and the solvent (d_f) was also defined. In MD, d_s and d_f can continuously adjust in response to the configuration, and d_f is (on average) different for the hydrophilic and hydrophobic sides. Default values of $d_s = 0.51\sigma$ and $d_f = 0.8\sigma$ were chosen by extracting averages from MD, but calculations were also made using several different values to show that these parameters have a minimal effect on orientation proba-

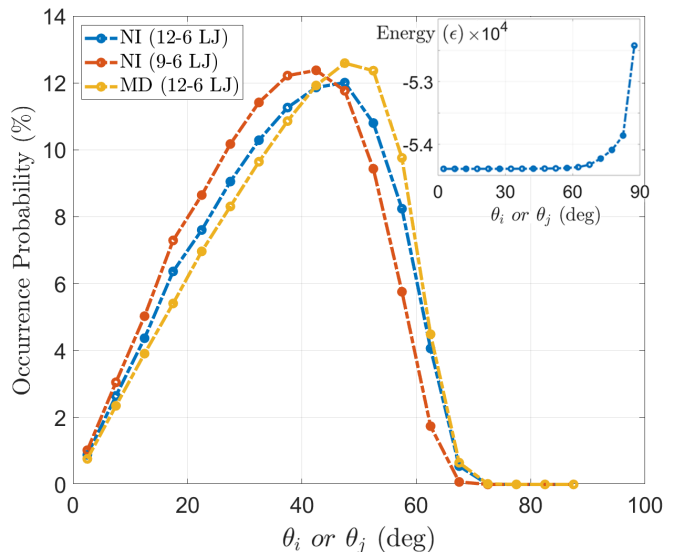


FIG. 2. The occurrence probability of orientations with different θ angles for Janus spheres in a dimer. The inset shows the energy landscape of the spheres configurations as a function of the polar angles. Lines are drawn to guide the eye.

bility distributions (see Supplemental Material). Otherwise, NI calculation parameters (e.g. surface and fluid densities) matched the values used in MD simulations. Given a configuration energy $E(\theta_j, \theta_i, \phi_i)$, the probability density can be determined using

$$p \propto \sin(\theta_j) \sin(\theta_i) \exp \left[-\frac{E}{k_B T} \right], \quad (2)$$

where k_B is Boltzmann’s constant and the number of ways a configuration of θ_i, θ_j can be obtained is proportional to $\sin(\theta_j) \sin(\theta_i)$. The Supplemental Material contains further detail regarding the NI method [45].

Potential effect - Fig. 2 compares the occurrence probability of polar angles calculated using MD and NI methods. The curves are broadly similar, and in particular the maximum occurrence probability occurs at very similar angles for the MD simulations and the NI calculation with a matching hard-sphere potential. The likely reasons for discrepancies between these plots are the known minor differences between MD and NI models, i.e. the fixed values of d_s and d_f and the sharp boundary between hemispheres in the NI model. For the soft-sphere potential, the probability distribution shifts slightly toward smaller angles.

To further understand these probability distributions, consider the calculated energy for the interaction between the two spheres (inset to Fig. 2) which is approximately constant for all configurations with $\theta_{i,j} < 60^\circ$. In this region, the reason for variation in occurrence probability is the lower configurational entropy (due to smaller surface area) near the poles. This is characteristic of potentials

which have little or no dependence on orientation, representing short-range interactions [25]. In contrast, approaches which use geometrically rigorous long-range interactions (electrostatic or DLVO) produce continuously varying potential landscapes [37, 38].

At $\theta > 60^\circ$, the interaction energy gradually increases, producing a sharp decline in the probability distribution for $60^\circ < \theta_{i,j} < 90^\circ$. This decline is not present when using a Kern-Frenkel type potential. In those cases, the maximum probability is found adjacent to the step function (at $\theta_{i,j} \approx 90^\circ$ for hemispheres), where the configurational entropy is greatest. Labbé-Laurent and Dietrich [40] derived a geometrically rigorous potential for a Janus dimer interacting via Casimir forces, which produced a similar combination of constant and varying potentials as in Fig. 2 inset, albeit without solvent.

The main reason for the increase in energy over the range $60^\circ < \theta_{i,j} < 90^\circ$ is that there is no solvent in the region near the point of closest approach between the spheres. It is energetically favourable for the hydrophobic surfaces to be shielded from the solvent near this contact point. The volume in which there is no fluid (an ‘exclusion zone’) is determined by d_f . The polar angle at which a sphere’s hydrophilic side enters this exclusion zone (and thus the hydrophobic side is not optimally hidden from the fluid) is $\theta_{i,j} = 90^\circ - \arccos(\frac{R+d_s/2}{R+d_f})$ (see Supplemental Material [45]), or $\theta_{i,j} = 72^\circ$ for our parameters, which matches well with Figs. 1(b) and 2. The precise shape of these distributions additionally depends on the form and range of the interaction potential.

The shift of the probability distribution to lower polar angles when using a soft-sphere (9-6) potential can be explained by the increased importance of long range interactions. For example, the minimum of the soft potential occurs at a larger radius than for the 12-6 potential. Increasing the range of the potential decreases the polar angle required for the hydrophilic side to be affected by the exclusion zone, thereby producing a decline in probability at lower polar angles.

Temperature was varied between $1.1 \epsilon/k_B$ and $1.5 \epsilon/k_B$ to study the effect on JP orientation. Fig. 3(a) shows polar angle probability distributions for two different temperatures calculated using both MD (via repeated simulations) and NI (using Eq. 2). At higher temperatures, the spheres spend more time in high energy orientations ($\theta_{i,j} > 60^\circ$) even up to unfavourable angles between 75° and 80° . Figure 3(b) indicates the expected value of $\theta_{i,j}$ at different temperatures. The results and trends from the MD and NI methods match closely, with a small difference possibly caused by fluid layering in MD (discussed further below).

To study the effect of hydrophobicity on orientation, the hydrophobic interaction strength was varied from $A_o = 0.05$ to 0.25ϵ at the default temperature ($1.1 \epsilon/k_B$). This produces very similar changes in the overall proba-

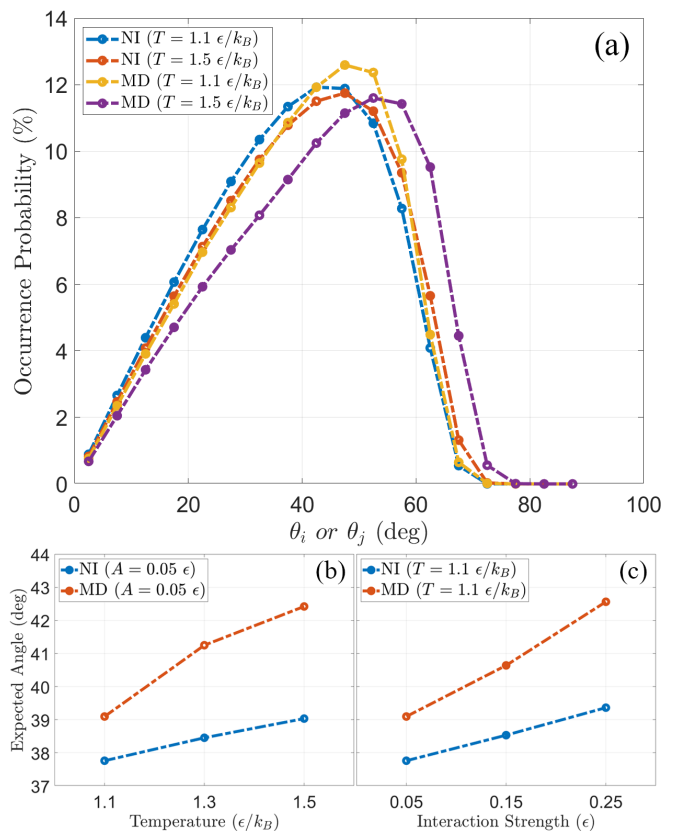


FIG. 3. (a) Occurrence probability as a function of polar angle for Janus spheres in a dimer at different temperatures ($R = 10 \sigma$). Lines are drawn to guide the eye. (b) and (c), expected value of the polar angle as a function of temperature and hydrophobicity, respectively.

bility distribution to variations in temperature (Fig. 3(a); see Supplemental Material [45]) and similar trends in the expected value of $\theta_{i,j}$ (Fig. 3(c)) albeit for a different reason. As the hydrophobicity decreases, the energy of the fluid-hydrophobic interactions becomes more negative which allows the hydrophobic sides of the spheres to be more exposed to the solvent atoms. Nonetheless, the spheres avoid forming orientations with polar angles higher than 70° .

While the NI calculations showed little dependence on the azimuthal angle (see the Supplemental Material [45]), an unexpected variation in probability was observed for MD results. As shown in Fig. 4, smaller values of $\Delta\phi$ are favoured. Data for two different temperatures (Figs. 4(a) and (b)) suggest that this variation is greater at higher temperature. This result can be explained by layering of solvent atoms around the spheres, which shows less ordering at smaller $\Delta\phi$ angles, increasing the entropy of the system. The free energy for orientations with smaller $\Delta\phi$ is therefore lower, and decreases with increasing temperature.

The layering can be observed in Fig. 4(c), which shows the spatial distribution of solvent atoms close to hy-

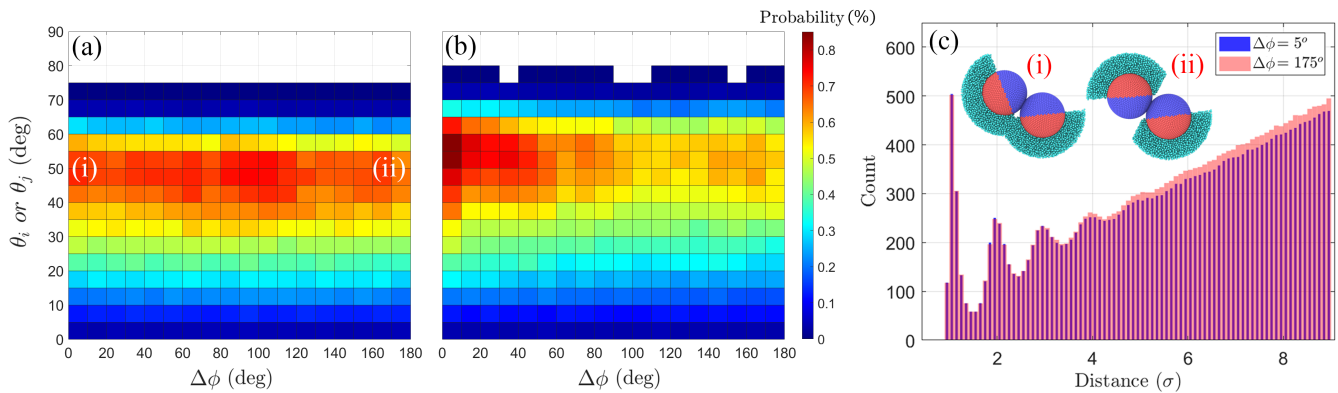


FIG. 4. The occurrence probability for dimer orientations in MD simulations ($A = 0.05 \epsilon$, $R = 10 \sigma$) at (a) $T = 1.1 \epsilon/k_B$, and (b) $T = 1.5 \epsilon/k_B$. (c) The spatial distribution of solvent atoms near the hydrophilic sides of JPs at $\Delta\phi = 5^\circ$ and $\Delta\phi = 175^\circ$. Insets, which represent the orientations from (a) at the corresponding equivalence labels, illustrate regions of layered solvent atoms used in the histogram. (ii) does not cover a full semi-circle to maintain equivalence with (i), which has an overlapping region.

drophilic surfaces for $\Delta\phi = 5^\circ$ and $\Delta\phi = 175^\circ$ when $55^\circ < \theta_i, \theta_j < 60^\circ$. The first three layers of solvent atoms are approximately the same for both cases, while the fourth and fifth peaks are somewhat stronger at $\Delta\phi = 175^\circ$. The insets to Fig. 4(c) illustrate the reason for this difference. At low $\Delta\phi$, the hydrophilic sides are close to each other so that regions of adjacent layered solvent overlap. Layers are observed at short range ($\lesssim 3 \sigma$) but the particles each influence longer range ordering of solvent adjacent to their neighbour. At higher $\Delta\phi$, the hydrophilic faces are further away from each other and the layering of solvent atoms is not disturbed by the neighbouring sphere. Near the hydrophobic faces, the range of ordered solvent atoms is much shorter and there is negligible contribution to ordering.

To conclude, our calculations using two independent methods have yielded consistent results for the favoured orientations of a dimer of amphiphilic JPs interacting via Lennard-Jones potentials in a solvent. The most favoured configurations are at polar angles between 40 and 55°. Pole-to-pole configurations are unfavoured due to orientational entropy and the short-range nature of the potential, while orientations near 90° are energetically unfavourable due to solvent exclusion between the particles. MD revealed that dynamic changes in the separation between particles and solvent atoms have a small effect on orientation probabilities, as do the details of the boundary between hemispheres. MD also showed that solvent ordering can break the degeneracy with respect to $\Delta\phi$. The NI method, which directly calculates the interaction energy, could be extended to ranges of practically important parameters, such as different potentials or non-hemispherical patches. Considering the role of orientational entropy, these methods should be particularly useful for designing patches which yield desired ‘floppy bonds’ geometries. The calculation efficiency of these methods suggest that they could be extended to study

clusters, and then used to find simplified yet accurate potentials for simulating many-particle structures.

This research was funded by The MacDiarmid Institute for Advanced Materials and Nanotechnology, and simulations were run on the NeSI Mahuika and Māui Clusters, part of the Centre for eResearch hosted by the University of Auckland.

-
- [1] L. M. Bergström, Application of Thermodynamics to Biological and Material Science **11**, 289 (2011).
 - [2] Z. Yang, A. H. Muller, C. Xu, P. S. Doyle, J. M. DeSimone, J. Lahann, F. Sciortino, S. Glotzer, L. Hong, D. A. Aarts, *et al.*, *Janus particle synthesis, self-assembly and applications* (Royal Society of Chemistry, 2012).
 - [3] E. Poggi and J.-F. Gohy, Colloid and Polymer Science **295**, 2083 (2017).
 - [4] M. N. Popescu, Langmuir **36**, 6861 (2020).
 - [5] A. Perro, S. Reculosa, S. Ravaine, E. Bourgeat-Lami, and E. Duguet, Journal of Materials Chemistry **15**, 3745 (2005).
 - [6] A. Walther and A. H. Müller, Soft Matter **4**, 663 (2008).
 - [7] A. Walther and A. H. Muller, Chemical Reviews **113**, 5194 (2013).
 - [8] Q. Chen, J. K. Whitmer, S. Jiang, S. C. Bae, E. Luijten, and S. Granick, Science **331**, 199 (2011).
 - [9] K.-H. Roh, D. C. Martin, and J. Lahann, Nature Materials **4**, 759 (2005).
 - [10] S. Jiang, Q. Chen, M. Tripathy, E. Luijten, K. S. Schweizer, and S. Granick, Advanced Materials **22**, 1060 (2010).
 - [11] Z. Preisler, T. Vissers, G. Munao, F. Smalenburg, and F. Sciortino, Soft Matter **10**, 5121 (2014).
 - [12] N. Safaie and R. C. Ferrier Jr, Journal of Applied Physics **127**, 170902 (2020).
 - [13] J. Zhang, B. A. Grzybowski, and S. Granick, Langmuir **33**, 6964 (2017).
 - [14] J. Zhang, E. Luijten, and S. Granick, Annual Review of Physical Chemistry **66**, 581 (2015).

- [15] M. F. Hagan, O. M. Elrad, and R. L. Jack, *The Journal of Chemical Physics* **135**, 104115 (2011).
- [16] B. A. Grzybowski, K. Fitzner, J. Paczesny, and S. Granick, *Chemical Society Reviews* **46**, 5647 (2017).
- [17] G. Rosenthal, K. E. Gubbins, and S. H. Klapp, *The Journal of Chemical Physics* **136**, 174901 (2012).
- [18] G. Munao, Z. Preisler, T. Vissers, F. Smalenburg, and F. Sciortino, *Soft Matter* **9**, 2652 (2013).
- [19] Z.-W. Li, Z.-Y. Lu, Z.-Y. Sun, and L.-J. An, *Soft Matter* **8**, 6693 (2012).
- [20] F.-F. Hu, Y.-W. Sun, Y.-L. Zhu, Y.-N. Huang, Z.-W. Li, and Z.-Y. Sun, *Nanoscale* **11**, 17350 (2019).
- [21] M. M. Moghani and B. Khomami, *Soft Matter* **9**, 4815 (2013).
- [22] L. Baran, M. Borówko, and W. Rżysko, *The Journal of Physical Chemistry C* (2020).
- [23] I. Kretzschmar and J. H. K. Song, *Current Opinion in Colloid & Interface Science* **16**, 84 (2011).
- [24] Y. Iwashita and Y. Kimura, *Soft Matter* **10**, 7170 (2014).
- [25] H. Shin and K. S. Schweizer, *Soft Matter* **10**, 262 (2014).
- [26] Q. Chen, J. Yan, J. Zhang, S. C. Bae, and S. Granick, *Langmuir* **28**, 13555 (2012).
- [27] Y. Iwashita and Y. Kimura, *Soft Matter* **9**, 10694 (2013).
- [28] X. Mao, Q. Chen, and S. Granick, *Nature Materials* **12**, 217 (2013).
- [29] W. L. Miller and A. Cacciuto, *Physical Review E* **80**, 021404 (2009).
- [30] F. Sciortino, *La Rivista del Nuovo Cimento* **42**, 511 (2019).
- [31] Y. Wang, Y. Wang, D. R. Breed, V. N. Manoharan, L. Feng, A. D. Hollingsworth, M. Weck, and D. J. Pine, *Nature* **491**, 51 (2012).
- [32] Q. Chen, S. C. Bae, and S. Granick, *Nature* **469**, 381 (2011).
- [33] F. Sciortino, A. Giacometti, and G. Pastore, *Physical Review Letters* **103**, 237801 (2009).
- [34] F. Smalenburg and F. Sciortino, *Nature Physics* **9**, 554 (2013).
- [35] L. Hong, A. Cacciuto, E. Luijten, and S. Granick, *Langmuir* **24**, 621 (2008).
- [36] N. Kern and D. Frenkel, *The Journal of Chemical Physics* **118**, 9882 (2003).
- [37] L. Hong, A. Cacciuto, E. Luijten, and S. Granick, *Nano Letters* **6**, 2510 (2006).
- [38] R. Hieronimus, S. Raschke, and A. Heuer, *The Journal of Chemical Physics* **145**, 064303 (2016).
- [39] A. Squarcini, A. Maciołek, E. Eisenriegler, and S. Dietrich, *Journal of Statistical Mechanics: Theory and Experiment* **2020**, 043208 (2020).
- [40] M. Labbé-Laurent and S. Dietrich, *Soft Matter* **12**, 6621 (2016).
- [41] D. Baowan and J. M. Hill, *Advances in Mechanical Engineering* **8**, 1687814016677022 (2016).
- [42] D. Baowan, B. J. Cox, T. A. Hilder, J. M. Hill, and N. Thamwattana, *Modelling and mechanics of carbon-based nanostructured materials* (William Andrew, 2017).
- [43] S. Plimpton, *Journal of Computational Physics* **117**, 1 (1995).
- [44] A. Stukowski, *Modelling and Simulation in Materials Science and Engineering* **18**, 015012 (2009).
- [45] *See Supplemental Material at [URL will be inserted by publisher] for further details on MD and NI methods.*
- [46] T. Vissers, Z. Preisler, F. Smalenburg, M. Dijkstra, and F. Sciortino, *The Journal of Chemical Physics* **138**, 164505 (2013).
- [47] Y.-C. Li, N.-B. Zhang, Z. Wei, B.-Y. Li, M.-T. Li, and Y. Li, *Molecular Simulation* **45**, 759 (2019).
- [48] J. Xu, Y. Wang, and X. He, *Soft Matter* **11**, 7433 (2015).
- [49] Y. Kobayashi, N. Arai, and A. Nikoubashman, *Soft Matter* **16**, 476 (2020).
- [50] S. Safaei, S. C. Hendy, and G. R. Willmott, *Soft Matter* **16**, 7116 (2020).
- [51] S. Safaei, A. Y. Archereau, S. C. Hendy, and G. R. Willmott, *Soft Matter* **15**, 6742 (2019).
- [52] G. Willmott, *Physical Review E* **77**, 055302 (2008).
- [53] G. R. Willmott, *Physical Review E* **79**, 066309 (2009).
- [54] A. Kharazmi and N. V. Priezjev, *The Journal of Chemical Physics* **142**, 234503 (2015).
- [55] Z.-W. Li, Z.-Y. Lu, Y.-L. Zhu, Z.-Y. Sun, and L.-J. An, *RSC Advances* **3**, 813 (2013).
- [56] Z.-W. Li, Z.-Y. Lu, and Z.-Y. Sun, *Soft Matter* **10**, 5472 (2014).
- [57] Z.-W. Li, Y.-L. Zhu, Z.-Y. Lu, and Z.-Y. Sun, *Soft Matter* **12**, 741 (2016).
- [58] Z.-W. Li, Y.-L. Zhu, Z.-Y. Lu, and Z.-Y. Sun, *Physical Chemistry Chemical Physics* **18**, 32534 (2016).
- [59] Z.-W. Li, Y.-L. Zhu, Z.-Y. Lu, and Z.-Y. Sun, *Soft Matter* **14**, 7625 (2018).
- [60] Q.-Z. Zou, Z.-W. Li, Z.-Y. Lu, and Z.-Y. Sun, *Nanoscale* **8**, 4070 (2016).
- [61] Q.-Z. Zou, Z.-W. Li, Y.-L. Zhu, and Z.-Y. Sun, *Soft Matter* **15**, 3343 (2019).